Journal of *Marine Science and Engineering*

MDPI

Article

Coverage Optimization Framework for Underwater Hull Cleaning Robots Considering Non-Uniform Cavitation Erosion Characteristics

Yunlong Wang [1], Zhenyu Liang [1,*], Zhijiang Yuan [2] and Chaoguang Jin [1]

[1] School of Naval Architecture, Dalian University of Technology, Dalian 116024, China; yunlongw@dlut.edu.cn (Y.W.); jinchg@dlut.edu.cn (C.J.)
[2] Department of Navigation, Dalian Naval Academy, Dalian 116018, China; yuanyr0531@163.com
* Correspondence: liangzhenyu@mail.dlut.edu.cn

Abstract

Underwater robots demonstrate significant potential for hull biofouling removal. However, achieving uniform and damage-free cleaning remains a persistent challenge. The fixed arrangement of cleaning mechanisms, combined with the inherent non-uniformity of cavitation jet energy distribution, frequently results in inconsistent removal depths, leading to local over-cleaning or under-cleaning. To address this, this paper proposes an optimization framework to coordinate the robot's motion with its cleaning mechanism. First, the flow field dynamics of the cavitation nozzle are elucidated using the Stress-Blended Eddy Simulation (SBES) turbulence model. Based on the Computational Fluid Dynamic (CFD) data, a Gaussian mapping model is constructed to quantify the relationship between jet erosion efficiency and robotic motion parameters. Furthermore, to resolve the multi-objective coverage parameter optimization problem, an improved hybrid metaheuristic algorithm—the Composite Cycloid Subtraction-Average-Based Optimizer (CCSABO)—is introduced to determine the optimal synchronization of forward and lateral velocities. Numerical simulations demonstrate the framework's robustness across various fouling thickness scenarios and nozzle parameters. Notably, the CCSABO algorithm achieves a coverage rate of 99% and minimizes the uniformity index to 0.011, demonstrating superior consistency compared to traditional PSO and GWO methods. This improvement effectively mitigates the risk of hull damage while ensuring cleaning quality.

Keywords: coverage optimization; underwater hull cleaning robot; cavitation erosion model; cleaning uniformity

Check for updates

Academic Editor: Alon Gany

Received: 30 December 2025
Revised: 20 January 2026
Accepted: 22 January 2026
Published: 27 January 2026

Copyright: © 2026 by the authors. Licensee MDPI, Basel, Switzerland. This article is an open access article distributed under the terms and conditions of the Creative Commons Attribution (CC BY) license.

1. Introduction

After a long voyage at sea, various marine organisms such as shellfish and barnacles inevitably form on the ship hull surface [1]. The fouling layer leads to increased surface roughness, enhanced resistance, and, consequently, additional time costs and fuel consumption [2]. Traditional manual cleaning methods, which rely on divers, are economically burdensome and inefficient and pose severe safety risks. Consequently, the development of autonomous underwater solutions for ship hull maintenance has become an imperative research focus [3].

Recently, underwater robots have been extensively deployed for hull cleaning tasks [4,5]. Common cleaning methods include brush-type, high-pressure jet, and cavitation jet. For instance, Wang et al. designed a permanent magnet adhesion robot featuring a disk-shaped

cavitation cleaning device, utilizing a rotating gun to enhance cleaning uniformity [6]. Similarly, Chen et al. proposed a crawler-type robot equipped with a stern-mounted array of four vertical cavitation guns [7]. To synthesize the benefits of physical abrasion and hydraulic impact, Wei et al. developed a hybrid robot integrating a mechanical roller brush with a cavitation jet module, validating its feasibility through simulations [8]. Each cleaning method possesses distinct characteristics and limitations. Brush-based cleaning offers structural simplicity but suffers from low efficiency, frequent component wear, and a high risk of damaging the hull coating [9]. High-pressure jets require immense power and can strip anti-corrosion layers, compromising the vessel's integrity [10]. In contrast, cavitation waterjet technology utilizes the collapse of cavitation bubbles to generate micro-jet impacts for fouling removal [11–13]. This non-contact approach significantly reduces the risk of surface damage. Consequently, cavitation jet-based robots offer superior versatility and safety compared to mechanical brushes and conventional high-pressure jets.

Despite these advantages, practical deployment faces significant hurdles arising from the complex coupling between the robotic carrier's motion constraints and the inherent non-uniformity of the cavitation jet. The complex curvature of ship hulls limits cleaning efficiency [14], and improper parameter control can lead to excessive energy deposition, damaging the anti-fouling paint [15]. To mitigate these issues, researchers have explored various optimization strategies. Mahmud et al. utilized NSGA-III and MOPSO algorithms to plan optimal cleaning routes [16], while Anh et al. applied reinforcement learning and deep convolutional neural networks to identify fouling conditions and automate path planning [17]. Similarly, Ghanta et al. employed NSGA-II to optimize sweeping speeds and angles for uniform hydro-blasting [18]. However, current optimization strategies primarily address global path planning, overlooking the local non-uniform distribution of jet energy. In practice, cleaning quality is highly sensitive to hydrodynamic control parameters, such as the standoff distance and jet incidence angle [19]. Neglecting these factors can lead to suboptimal performance. Recent experimental studies have highlighted the importance of dynamic interactions; for example, Madanipour and Najafi [20] analyzed the vibrational forces of rotating brushes to reduce surface damage, and Fang et al. [21] experimentally determined optimal control parameters for cavitation jets. Nevertheless, a unified framework that integrates micro-scale hydrodynamic mechanisms with macro-scale robotic coverage strategies is still lacking.

Recent studies have successfully combined CFD data with optimization algorithms in other fields. For instance, Zhang et al. optimized ejector designs using PSO [22], and Apte et al. characterized cavitating flows using genetic algorithms [23]. However, applying such frameworks to the specific non-uniformity of hull cleaning remains underexplored. To address this gap, this paper proposes a holistic optimization framework for a lateral reciprocating cavitation cleaning robot. Unlike previous studies that rely on simplified erosion models, we employ the high-fidelity Stress-Blended Eddy Simulation (SBES) model to resolve the transient cavitation cloud distribution. Based on the CFD data, a Gaussian-based cleaning efficiency function is established. Furthermore, to solve the complex multi-objective optimization problem where traditional algorithms often trap in local optima, a Composite Cycloid Subtraction-Average-Based Optimizer (CCSABO) is introduced. This framework aims to balance cleaning uniformity and efficiency.

The main contributions can be summarized as follows:

(1) Design of a Reciprocating Lateral Cleaning Mechanism: A specialized cleaning device featuring a sliding rail and three pairs of Helmholtz self-excited oscillation nozzles is designed. This mechanism enables lateral cleaning, allowing the robot to traverse on clean surfaces, thereby enhancing adhesion stability and locomotion reliability compared to traditional aft-mounted designs.

(2) Cavitation Modeling using SBES: The SBES turbulent model, coupled with the Schnerr-Sauer cavitation model, is utilized to simulate the turbulent cavitation flow. This approach accurately identifies the optimal standoff distance based on cavitation cloud evolution. A Gaussian mapping model is then developed to quantify the non-uniform erosion characteristics, serving as the physical basis for coverage optimization.

(3) Optimization Strategy via CCSABO: A novel coverage strategy is modeled to maximize uniformity. The control parameters are optimized using the proposed CCSABO algorithm. Comparative simulations demonstrate that this approach significantly enhances the coverage rate and uniformity index, offering a robust solution for automated hull maintenance.

The remainder of this paper is organized as follows: Section 2 presents the mechanical design of the robot system. Section 3 details the numerical simulation of the cavitation jet and establishes the cleaning coverage model. Section 4 describes the CCSABO optimization process. Section 5 discusses the simulation results under various scenarios, and Section 6 concludes the paper.

2. System Model

2.1. Robot System and Physical Constraints

The overall mechanical architecture of the robot is illustrated in Figure 1, with key dimensional specifications detailed in Table 1. The system comprises six primary subsystems: the main frame, the mobile and adhesion mechanism, the cleaning device, the sensor system, the control unit, and the buoyancy module.

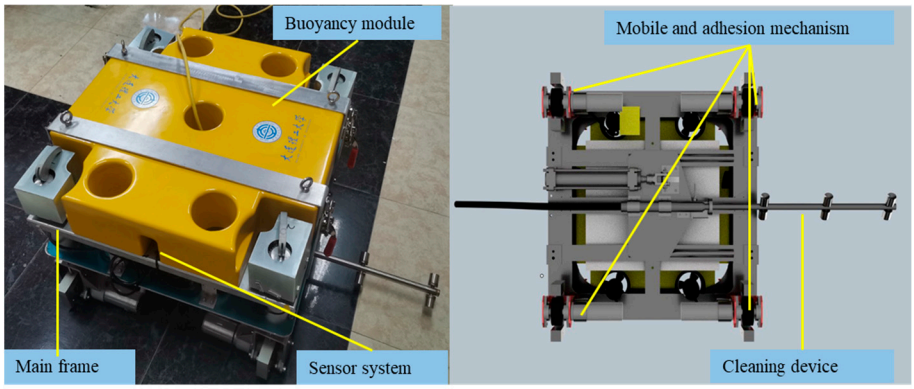


Figure 1. Mechanical structure of the robot.

Table 1. Specifications of the cleaning robot.

Parameter	Value	Unit
Size	700 × 700 × 470	mm
Mass	65	kg
Buoyancy	600	N
Maximum climbing speed	0.5	m/s
Maximum sailing depth	50	m
Cleaning width	400	mm

This robot defines the feasible search space for the subsequent CCSABO optimization. The robot's structure (e.g., cleaning width) and motion limits (e.g., maximum forward velocity) determine the limits for the optimization variables.

The reciprocating cavitation jet cleaning device is shown in Figure 2a, with key specifications detailed in Table 2. The spray gun can be extended out of the robot to achieve

lateral cleaning. Three pairs of Helmholtz nozzles are mounted on the spray gun. The nozzle-to-wall standoff distance can be manually adjusted. Here the specifications of the cleaning device determine the parameters for subsequent CFD modeling and optimization.

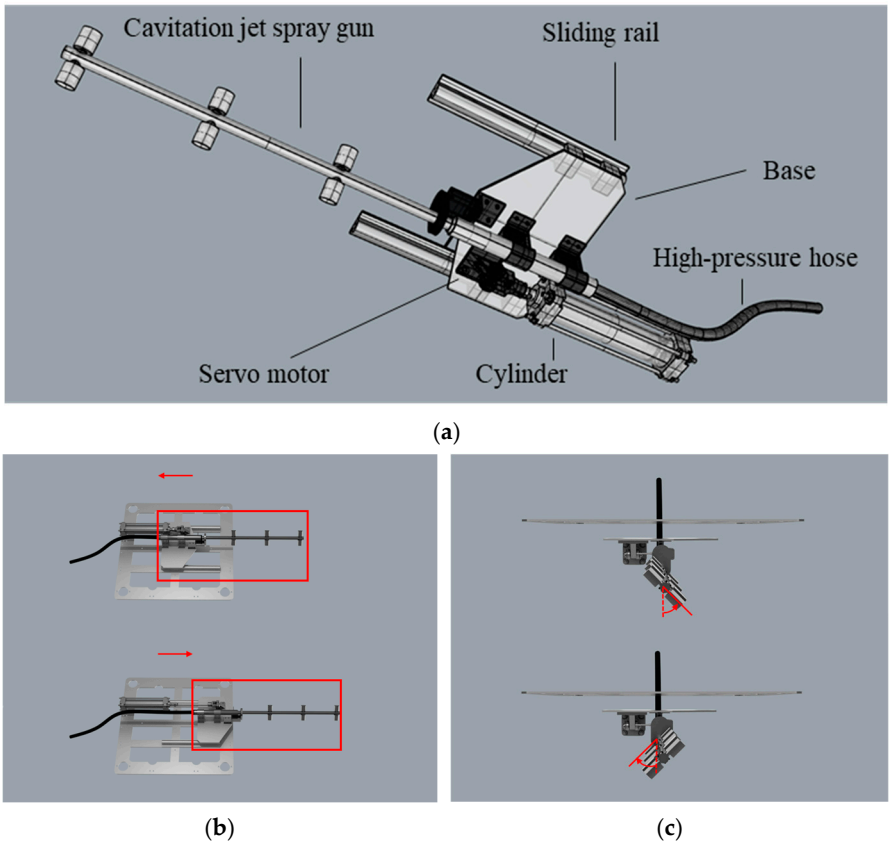


Figure 2. Mobile and rotating spray gun structure. (**a**) Mechanical structure of cleaning device; (**b**) Movement of spray gun, the section within the red box can be moved in the direction of the arrow; (**c**) Rotation of spray gun.

Table 2. Specifications of the cleaning device.

Parameter	Value	Unit
Length of the spray gun	400	mm
Cylinder stroke	200	mm
Standoff distance	40~100	mm
Maximum Reciprocating speed	3	m/s
Number of nozzles	6	-

As illustrated in Figure 2b, the nozzle assembly is secured to the base, which reciprocates along the sliding rail. Unlike traditional underwater cleaning robots that typically employ fixed nozzle configurations—often resulting in limited coverage width and non-uniform removal—the proposed sliding mechanism enables the nozzle to reciprocate while the robot moves forward. This compound motion significantly expands the effective swath width and promotes uniform cleaning coverage across the target surface.

Furthermore, a rotational adjustment mechanism was integrated, as shown in Figure 2c. This feature allows for the dynamic adjustment of the nozzle's angle of attack. For instance, the cavitation jet can be oriented to strike the root of biofouling organisms, facilitating multi-angle accessibility for stubborn fouling and thereby enhancing overall cleaning efficiency.

2.2. Lateral Coverage Model

The coverage path planning strategy for the ship hull surface is illustrated in Figure 3. Traditional underwater cleaning robots typically employ ventral or anteriorly mounted cleaning mechanisms. This configuration compels the robot to traverse uncleaned surfaces, as depicted in Figure 3a. In these areas, thick layers of biofouling create a significant gap between the magnetic wheels and the steel hull, drastically reducing magnetic adhesion.

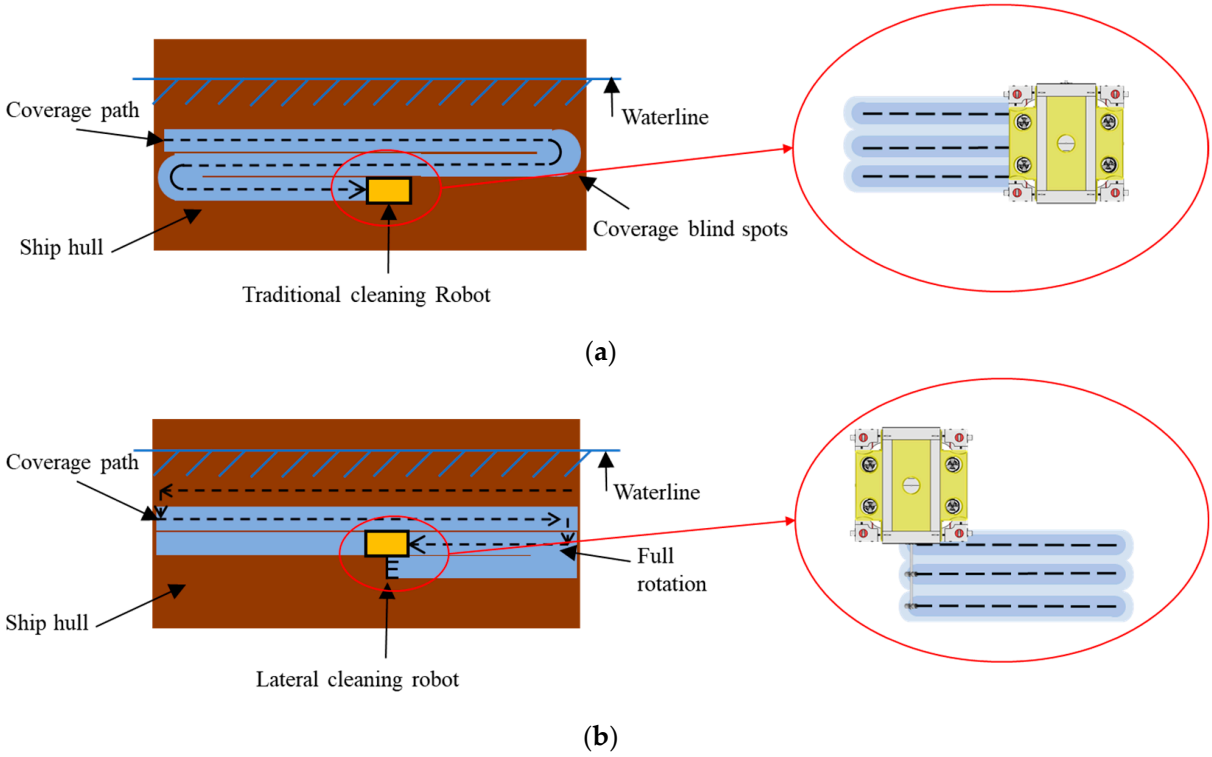


Figure 3. Two different cleaning coverage methods. (**a**) Traditional cleaning coverage; (**b**) Lateral cleaning coverage. Detailed coverage patterns are shown in the red circles.

To address these limitations, a lateral cleaning strategy is proposed, as shown in Figure 3b. By utilizing a cleaning lance extended laterally from the chassis, the robot is able to navigate along the previously cleaned swath. This approach ensures direct contact between the wheels and the clean hull surface, thereby maximizing magnetic adhesion and enhancing locomotion stability. Additionally, leveraging the robot's omnidirectional maneuverability, the system can adjust its orientation to minimize coverage blind spots, ensuring comprehensive cleaning.

The combination of a lateral coverage model with a reciprocating device enables uniform coverage of large areas and provides a physical basis for subsequent optimization.

2.3. Optimization Framework

As illustrated in Figure 4, the framework synthesizes the physical robotic system with computational models to address cleaning uniformity:

(1) Physical Constraint Layer: Illustrates the developed wall-climbing robot featuring the novel lateral reciprocating mechanism. The mechanical design defines the kinematic constraints and feasible ranges for the forward velocity and lateral sweep velocity. The nozzle parameters determine the computational domain settings for subsequent CFD modeling.

(2) Hydrodynamic Modeling Layer: Resolves the cavitation jet flow field using SBES and establishes a quantitative relationship between erosion depth and energy distribution via Gaussian mapping for subsequent cleaning coverage optimization.
(3) Cooperative Optimization Layer: Inputs both the mechanical kinematic constraints and the hydrodynamic erosion model into the CCSABO. The algorithm iteratively determines the optimal velocity synchronization strategy, achieving maximized coverage and uniformity within the hardware's operational limits.

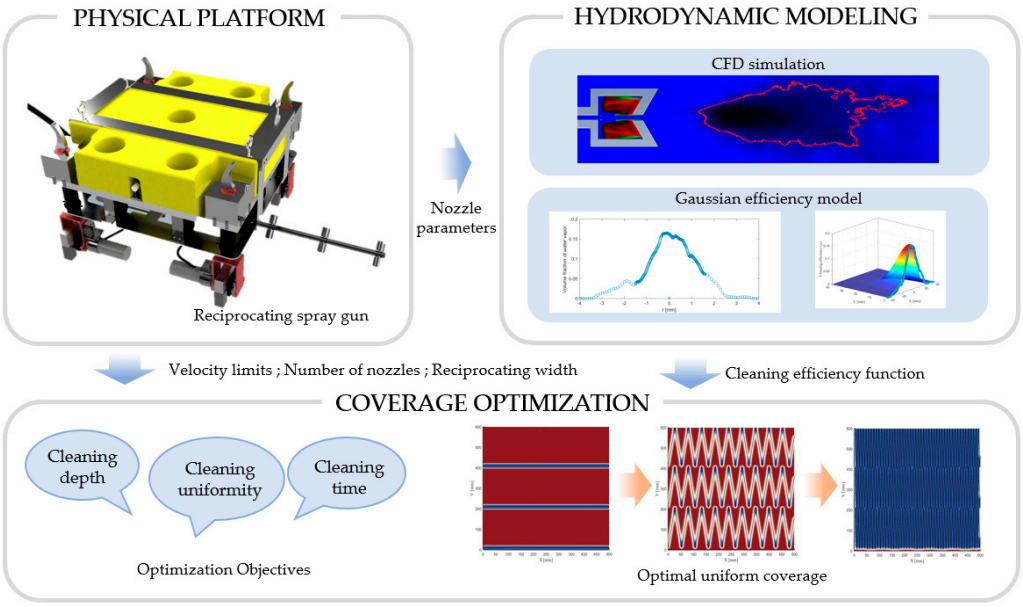


Figure 4. The collaborative optimization framework integrating the robotic platform and hydrodynamic characteristics.

Based on the robot specifications, parameters such as kinematic constraints and nozzle arrangement were established for the subsequent simulation models. The proposed framework maintains high generalizability, adapting to a new platform requires only updating the physical parameters, without altering the core algorithm.

3. Cavitation Jet Cleaning Coverage Model

3.1. Non-Uniform Cavitation Erosion Characteristics

In this study, we investigated the non-uniform cavitation erosion characteristics of a Helmholtz nozzle via numerical simulation. Subsequently, a cleaning efficiency function was established based on the hydrodynamic simulation results. These results act as input parameters for the objective function in Section 4.

3.1.1. Cavitation Jet Model

Given the axisymmetric geometry of the nozzle, the internal flow field can be simplified to a two-dimensional (2D) axisymmetric model to facilitate simulation and calculation [24,25]. Conventional turbulence models, such as Reynolds-averaged Navier–Stokes (RANS), often exhibit limitations in accuracy when predicting unsteady cavitation behaviors. Consequently, density-corrected models are frequently required to modify turbulent viscosity [26,27]. Although Large Eddy Simulation (LES) offers high-resolution capture of cavitation dynamics, its application is often constrained by the prohibitive computational cost associated with the requirement for extremely fine meshes. The Stress-Blended Eddy Simulation (SBES) model [28] serves as an efficient alternative. It employs RANS within the near-wall boundary layer to minimize computational load while utilizing LES in shear

flow regions for precise turbulence prediction. This hybrid approach effectively balances boundary layer accuracy with the resolution of transient vortex structures, providing enhanced turbulence fidelity while significantly reducing grid requirements [29]. In this paper, numerical simulations of the cavitation jet were conducted using ANSYS Fluent 15.0. The simulation framework incorporated the Mixture model for multiphase flow, coupled with the SBES turbulence model and the Schnerr-Sauer cavitation model.

The Helmholtz nozzle, fabricated from high-strength stainless steel, features a standard 120° impinging edge geometry [30,31], as depicted in Figure 5. Detailed geometric parameters, including the diameter and length of each section, are listed in Table 3. The computational domain, along with the boundary conditions and mesh configuration, is illustrated in Figure 6. A no-slip wall condition was applied to the nozzle surface. The inlet was defined as a pressure inlet at 2 MPa [32], while the outlet was set as a pressure outlet corresponding to a hydrostatic pressure depth of 5 m (150,325 Pa). A trimmed mesh strategy was employed, with local refinement applied along the jet axis to accurately capture the cavitation region. Transient simulations were conducted with a time step of 10^{-5} s, allowing for a maximum of 20 iterations per time step to ensure convergence.

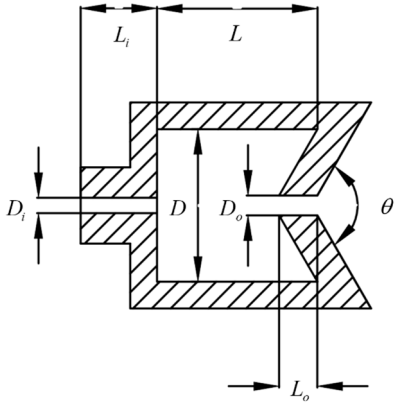


Figure 5. The structure of the Helmholtz nozzle.

Table 3. The dimensions of the Helmholtz nozzle.

Parameters	Symbol	Parameters	Units
Inlet pipe diameter	D_i	2	mm
Resonant cavity diameter	D	20	kg
Minimum throat diameter	D_o	2.6	N
Resonant cavity length	L	20	m/s
Minimum throat length	L_i	11	m
Export lip length	L_o	10	mm
Exit spread angle	θ	120	°

A two-dimensional coordinate system was established with the origin located at the nozzle inlet, the x-axis aligned with the central axis, and the y-axis representing the radial direction. To verify grid independence, four monitoring points were selected along the x-axis to record the time-averaged vapor volume fraction. The coordinates are defined as: Point 1 (0.026, 0) m, Point 2 (0.050, 0) m, Point 3 (0.070, 0) m, and Point 4 (0.090, 0) m, as shown in Figure 6. Five distinct mesh resolutions were generated to analyze variations in the vapor volume fraction at each monitoring point, is illustrated in Figure 7. The element numbers of the five mesh configurations are 91 k, 185 k, 283 k, 374 k, and 482 k, respectively. Since direct experimental measurement of the internal nozzle flow is challenging, a self-evaluation method based on grid convergence was adopted. Results indicated that Mesh 1 and Mesh 2 significantly underestimated the vapor fraction at Points 2, 3, and 4 while

overestimating it at Point 1. In contrast, Meshes 3–5 demonstrated convergent behavior, showing minimal deviations in vapor fraction predictions across all monitoring locations. The average relative margin of the vapor volume fraction between Mesh 4 and Mesh 5 is less than 2%, indicating that the solution has achieved grid independence.

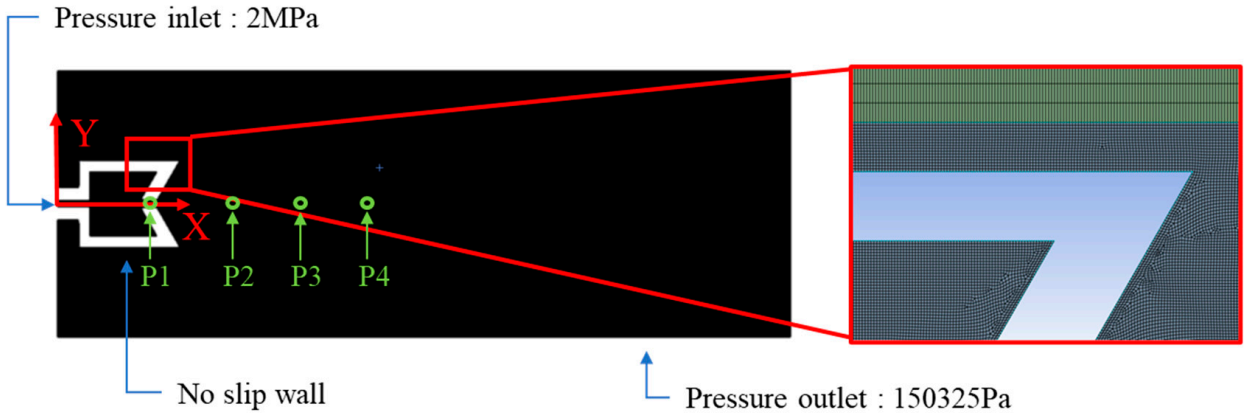


Figure 6. Mesh of fluid computational domain. Green dots represent monitoring locations, with detailed mesh configurations displayed within the red box.

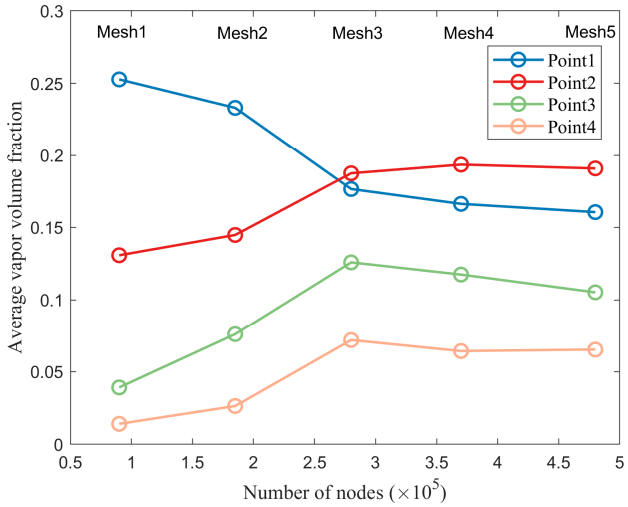


Figure 7. Mesh independence analysis.

To balance accuracy and computational efficiency, the Mesh 4 configuration was adopted. The global mesh size was set to 1×10^{-3} m. A refinement zone (0.15 times the global size, i.e., 1.5×10^{-4} m) was applied to critical regions, resulting in a total of 374,317 elements within the fluid domain.

Previous studies have established that cavitation jet erosion results from high-intensity impulsive pressure loads generated by the collapse of cavitation clouds upon the target surface [33]. Accordingly, in this study, the vapor volume fraction distribution is utilized to characterize the non-uniform profile of cavitation erosion. Furthermore, the optimal nozzle-to-wall standoff distance is determined by analyzing the evolution dynamics of the cavitation cloud.

Figure 8 illustrates the vapor phase fraction at various time instances, revealing the diffusive evolution of the cavitation cloud along the jet axis. As the cloud propagates away from the nozzle, it expands, sheds, collapses, and eventually dissipates. By superimposing 10,000 frames, a time-averaged vapor phase distribution over 0.1 s was obtained; image sharpening was subsequently applied to enhance contrast. Based on this distribution, the

cavitation coverage was modeled as a cone. This geometric approximation allows for the determination of the jet spread angle α and the optimal standoff distance d_1. Consequently, the effective coverage radius R of a single nozzle can be calculated as follows:

$$R = d_1 \tan \alpha \tag{1}$$

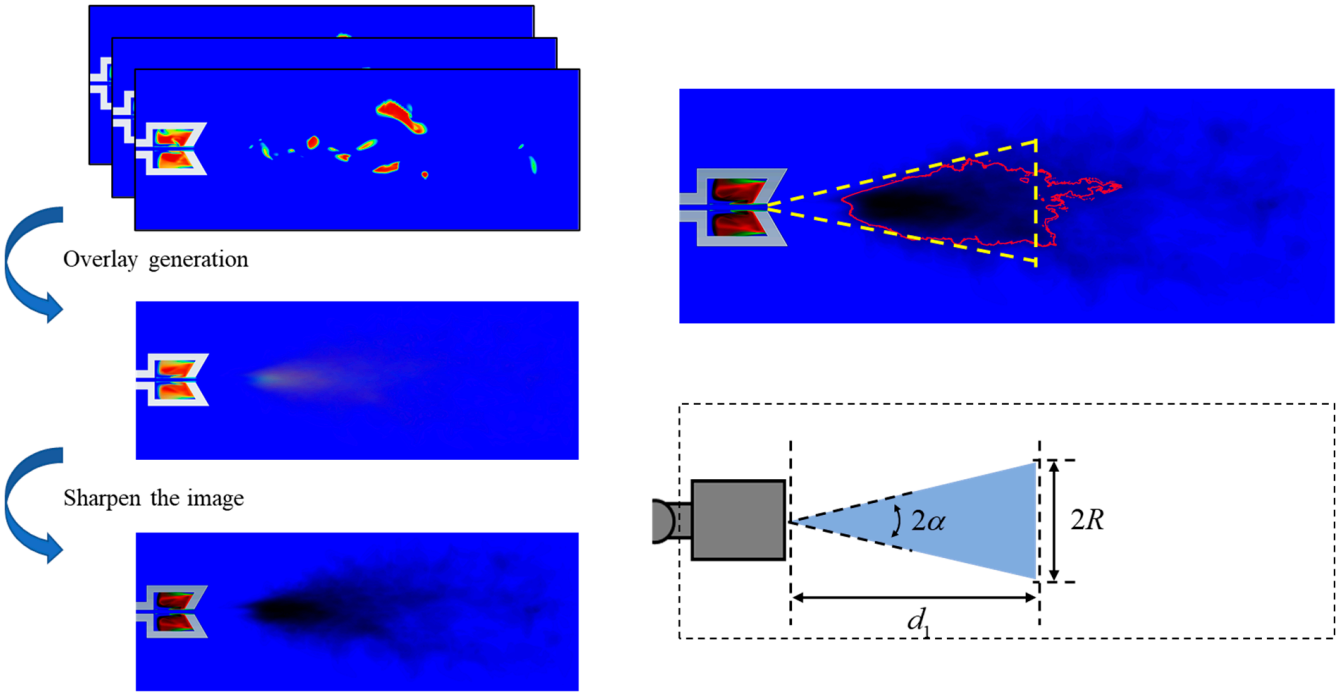


Figure 8. Time-averaged vapor fraction distribution derived from 10,000 frames. The yellow outline represents the jet range obtained from CFD simulation.

3.1.2. Cleaning Efficiency Function

The intensity distribution of the cavitation cloud exhibits significant spatial variation across the impact plane, necessitating a strategy for uniform coverage. Figure 9 illustrates the radial distribution of the cavitation volume fraction, indicating a higher vapor phase concentration near the nozzle axis. Time-averaging the vapor phase distribution over 0.1 s (derived from 10,000 frames) reveals a quasi-Gaussian profile characterized by a central depression. This suggests an annular region of maximum erosion, a finding consistent with established research on cavitation erosion patterns [19].

To achieve uniform and efficient cleaning, a mathematical model was established linking erosion depth, exposure duration, cleaning efficiency, and nozzle parameters. In practical applications, cleaning efficiency depends not only on cavitation intensity but also on factors such as jet incidence angle, impact pressure distribution, and the properties of the fouling material [21,34]. However, numerous studies have demonstrated that the primary mechanism driving erosion is cavitation collapse [19,35,36]. In this model, cleaning efficiency is estimated based on the vapor phase distribution; that is, a higher vapor phase fraction corresponds to a stronger cleaning effect. Therefore, a Gaussian function was employed to approximate the vapor phase distribution curve shown in Figure 9, thereby constructing a cleaning efficiency function $\mu(r)$, defined as:

$$\mu(r) = \mu_m \exp(-\frac{x^2}{2s^2}) \, , x \in [-R, R] \tag{2}$$

where μ_m represents the maximum cleaning efficiency (located at the jet center), x denotes the radial distance from the center within the coverage area, R signifies the maximum coverage radius of the jet, and s is the standard deviation of the Gaussian function.

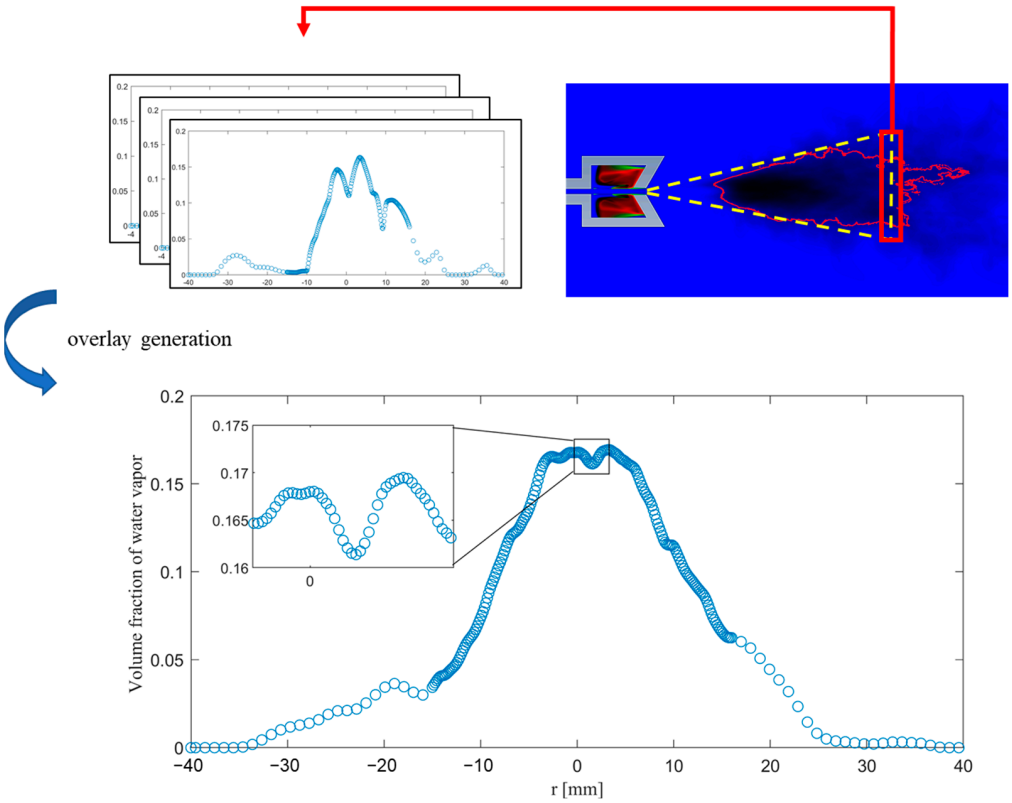


Figure 9. A total of 10,000 frames of vapor fraction images are overlaid. The red box represents the plane of intersection.

Based on the vapor phase distribution data $Vp \sim (v_1, v_2, v_3, \ldots v_n)$, the fitting objective is formulated as: $\min \sum_{i=1}^{n} \left[v_i - \mu_m \exp(-\frac{r^2}{2s^2}) \right]^2$. This optimization problem was solved using the least squares method, and the fitting result is illustrated in Figure 10.

The goodness of fit was rigorously evaluated using two statistical metrics:

(a) Root Mean Square Error (RMSE) = 0.0066: A value approaching zero indicates minimal deviation between the fitted curve and the observed data.

(b) Coefficient of Determination (R^2) = 0.9865: A value close to 1 demonstrates the high explanatory power of the model.

These results confirm the accuracy of the Gaussian model in characterizing the vapor distribution. Building upon the one-dimensional Gaussian curve and considering the axisymmetric nature of the nozzle, a corresponding two-dimensional Gaussian distribution surface was constructed using the formula:

$$\mu(r) = \mu_m \exp(-\frac{x^2 + y^2}{2s^2}) \, , \sqrt{x^2 + y^2} \in [-R, R] \tag{3}$$

This two-dimensional distribution effectively represents the spatial variation in cavitation intensity across the impact plane.

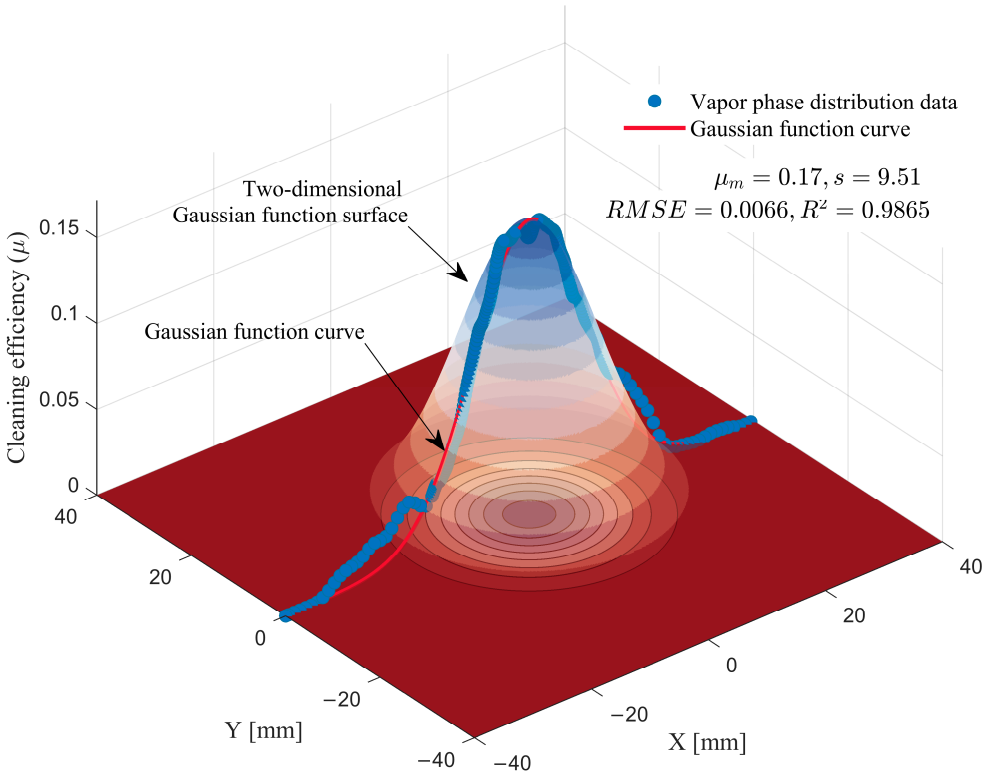


Figure 10. The cleaning efficiency of a nozzle.

3.2. Lateral Reciprocating Cleaning Coverage Model

Traditional hull cleaning robots typically employ fixed nozzles, which often limits both coverage uniformity and the total effective area. Addressing the dynamics of lateral motion and reciprocating mechanisms, this section develops a mathematical model for lateral reciprocating cleaning coverage. Furthermore, the factors influencing coverage uniformity and efficiency are analyzed to facilitate subsequent optimization.

3.2.1. Reciprocating Sweep Strategy

Figure 11 illustrates two distinct sweeping patterns: the line sweep strategy (Figure 11a) and the reciprocating sweep strategy (Figure 11b), where u and v denote the robot's forward velocity and the spray gun's lateral sweeping velocity, respectively. The line sweep strategy, commonly adopted in conventional robots, utilizes a linear array of nozzles for parallel coverage. However, due to the non-uniform coverage of individual nozzles (as demonstrated in Figure 10), this approach is prone to leaving uneven gaps or "blind spots" between adjacent paths. In contrast, this study proposes a reciprocating strategy based on the cavitation jet device introduced in Section 2.2. This method achieves a broader coverage area and superior uniformity. Although advantageous, the reciprocating strategy requires precise coordination between lateral and forward motions. For instance, a low lateral velocity v coupled with a high forward velocity u may result in triangular uncleaned regions at the path edges. Additionally, the reciprocating stroke must be synchronized with nozzle spacing to avoid redundant overlap. These critical parameters are analyzed in detail in the following subsection.

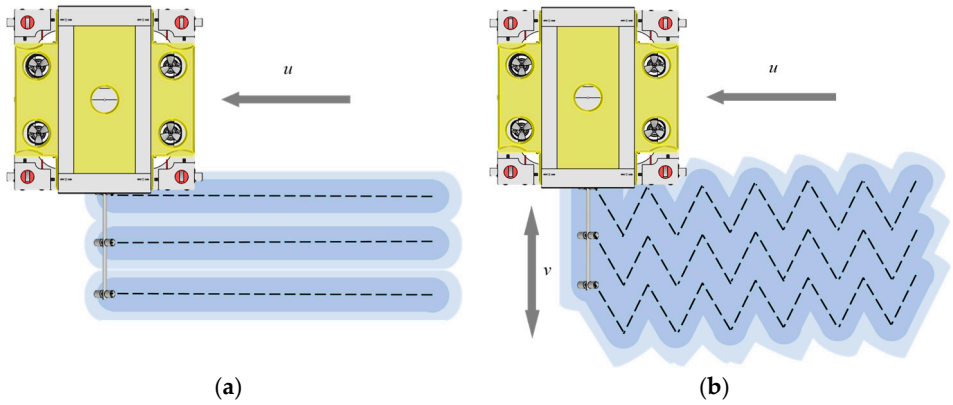


Figure 11. Comparison of two sweep strategies. (**a**) Line sweep strategy; (**b**) Reciprocating sweep strategy. Arrows indicate the movement direction of the robot and cleaning mechanism.

3.2.2. Parameters to Be Optimized

Based on the conical diffusion profile established in Section 3.1, the cleaning coverage of a three-nozzle gun is modeled as depicted in Figure 12. The system possesses two degrees of freedom: the lateral velocity v provided by the pneumatic cylinder and the forward velocity u provided by the robot platform. d_2 denotes the fouling thickness, while d_1, α, and R correspond to the parameters determined in Section 3.1. Practically, as the gun approaches the limit of its lateral stroke, it undergoes deceleration and buffering before reversing direction. However, for modeling simplicity, this motion is approximated as uniform.

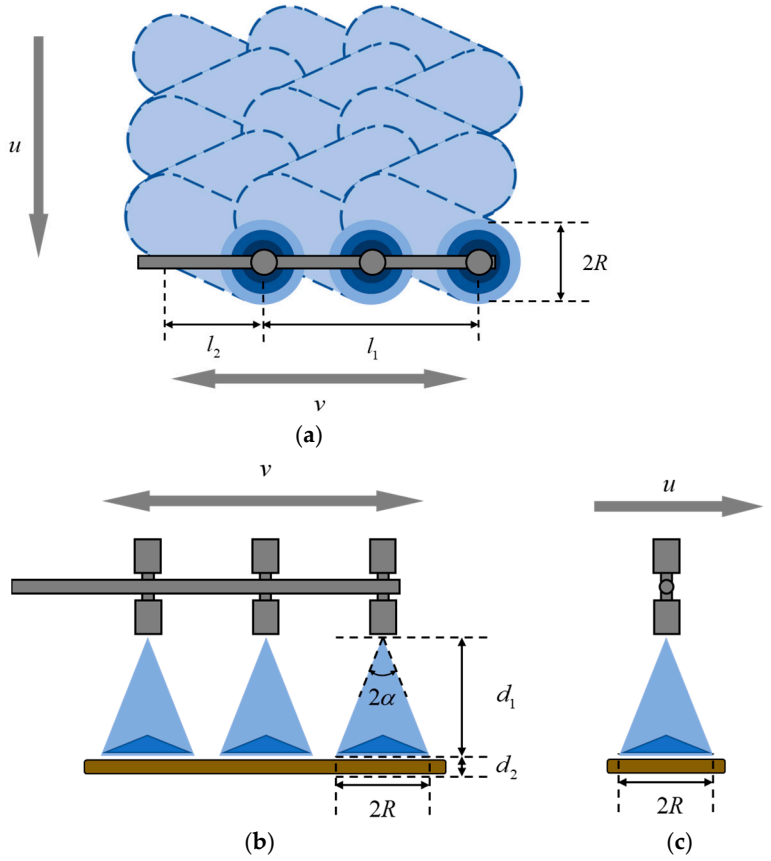


Figure 12. Reciprocating cleaning coverage model. (**a**) Top view; (**b**) front view; (**c**) side view. Arrows indicate the movement direction of the robot and cleaning mechanism.

Integrating the cleaning efficiency function derived in Equation (2), the effective cleaning depth $d_{clr}(r)$ is defined as:

$$d_{clr}(r) = \tau \int_t \mu(r) \tag{4}$$

$$d_{clr} \geq d_2 \tag{5}$$

where $d_{clr}(r)$ represents the thickness of the fouling removed at position r within time t (unit: mm). The coefficient τ relates cleaning efficiency to the actual material removal rate and depends on the specific properties of the marine fouling. To ensure effective cleaning, the condition Equation (5) must be satisfied across the entire target area.

As illustrated in Figure 12a, given a spray gun length l_1 and a cylinder stroke l_2, the effective cleaning width l is expressed as:

$$l = l_1 + l_2 \tag{6}$$

For a spray gun equipped with three nozzles, it is evident that setting the nozzle spacing $l_2 = \frac{l_1}{2}$ appropriately maximizes the coverage area while minimizing redundant sweeping.

To calculate the time required to cover a region of length L and width W, the specific sweeping kinematics must be considered. Regardless of whether a line or reciprocating sweep is used, the area is processed strip by strip; the primary differences lie in the turning time and the effective strip width. The total process time is calculated as follows:

(a) The time required to traverse a single strip of length L at velocity u is $\frac{L}{u}$.
(b) Although the robot must execute a turn at the end of each strip, for simplicity, a fixed turning time T_{turn} is assumed.
(c) The number of strips required to cover the width W given a cleaning width l is $ceil(\frac{W}{l})$, where the function $ceil(\bullet)$ returns the smallest integer greater than or equal to the input value.

Consequently, the total time consumption T_{clr} for the line sweep strategy is formulated as:

$$T_{clr} = \frac{L}{u} \cdot ceil(\frac{W}{l}) + T_{turn} \cdot \left[ceil(\frac{W}{l}) - 1\right] \tag{7}$$

To achieve the optimal cleaning depth $d_{clr}(r)$ and minimize the total cleaning time T_{clr}, the velocities u and v are selected as the key design variables for optimization.

4. Cleaning Coverage Optimization

4.1. Optimization Objectives

This section defines the specific optimization objectives and constructs a composite fitness function to formulate the optimization task as a minimization problem.

The primary objectives for optimizing the cleaning coverage are established as follows:

(a) Effective Cleaning Depth: The cleaning depth across the target area must meet or exceed the fouling thickness to ensure thorough removal of marine growth.
(b) Cleaning Uniformity: The process should exhibit high uniformity to prevent localized over-cleaning, which could potentially damage the hull substrate while avoiding under-cleaned areas.
(c) Cleaning Time: The total operational time should be minimized to maximize cleaning efficiency.

Note: While the coverage rate is frequently cited as a critical metric in related studies [37–39], it is not explicitly included as an independent variable in the fitness function of

this study. This is because the coverage rate is intrinsically dependent on cleaning uniformity and effective depth; therefore, optimizing these two parameters implicitly maximizes the coverage rate.

The global fitness function $f(x)$ is defined as:

$$\min f(x) = \sum_{i=1}^{3} k_{fi} \cdot f_i(x) \tag{8}$$

where k_{fi} denotes the weighting coefficient for each objective, and $f_i(x)$ $(i = 1, 2, 3)$ represents the individual fitness function corresponding to cleaning depth, uniformity, and cleaning time, respectively. The weights were determined based on the priority of engineering requirements, such as uniformity > depth accuracy > time efficiency. The optimization variables are subject to the constraints $u_{\min} \leq u \leq u_{\max}$ and $v_{\min} \leq v \leq v_{\max}$, where the subscripts min and max indicate the lower and upper bounds of the robot's forward velocity u and the cylinder's lateral velocity v.

To eliminate dimensional differences and allow for the weighting of indicators with disparate magnitudes, normalization is performed prior to the summation of $f_i(x)$, as defined by:

$$f_i(x) = \frac{f_i(x) - f_i(x)_{\min}}{f_i(x)_{\max} - f_i(x)_{\min}} \tag{9}$$

Through this normalization operation, the range of each sub-function $f_i(x)$ is constrained to the interval [0, 1], ensuring that the fitness coefficients k_{fi} can accurately reflect the relative importance of each optimization objective.

4.1.1. Cleaning Depth Fitness Function

To evaluate the cleaning efficacy, N_p sampling points are stochastically selected within the coverage area to measure the deviation between the actual cleaning depth $d_{clr}(p_i)$ at the i-th point and the target fouling thickness $d_{desired}$. The cleaning depth penalty function $f_1(x)$ is formulated as follows:

$$f_1(x) = \frac{1}{N_p} \sum_{i=1}^{N_p} \alpha \cdot (d_{desired} - d_{clr}(p_i)) \tag{10}$$

$$\alpha = \begin{cases} 1 & \text{if } d_{desired} > d_{clr}(p_i) \\ -0.5 & \text{if } d_{desired} < d_{clr}(p_i) \end{cases} \tag{11}$$

where α represents the penalty coefficient for the cleaning depth. The fitness function is designed with an asymmetric penalty mechanism: it imposes a severe penalty on insufficient cleaning ($d_{desired} > d_{clr}(p_i)$) to strictly ensure fouling removal while applying a more lenient penalty for over-cleaning ($d_{desired} < d_{clr}(p_i)$). This design prioritizes the effectiveness of fouling removal, treating the risk of substrate damage as a secondary constraint within permissible limits.

4.1.2. Cleaning Uniformity Fitness Function

To assess the uniformity of the cleaning coverage, the same stochastic sampling method described in Section 4.1.1 is employed to analyze variations in cleaning depth. Drawing upon the concept of fairness metrics proposed by Raj Jain [40], the uniformity fitness function $f_2(x)$ is defined as:

$$f_2(x) = 1 - \frac{[\sum_{i=1}^{N_p} d_{clr}(p_i)]^2}{N_p \cdot \sum_{i=1}^{N_p} d_{clr}(p_i)^2} \tag{12}$$

where the function values quantify the dispersion of individual cleaning depths relative to the mean, with a range of $[0, 1]$. As the cleaning depth across the sampled points becomes more consistent, the value of $f_2(x)$ approaches zero. Specifically, $f_2(x)$ reaches its global minimum of zero if and only if the cleaning depth is identical at all sampled points, indicating perfect uniformity.

4.1.3. Cleaning Time Fitness Function

The fitness function for cleaning time, $f_3(x)$, is derived directly from the total time consumption calculation in Equation (7):

$$f_3(x) = T_{clr} \tag{13}$$

By minimizing $f_3(x)$, the optimization process seeks to reduce the total operational duration, thereby maximizing the overall cleaning efficiency.

4.2. Composite Cycloid Subtraction-Average-Based Optimizer

Various metaheuristic algorithms have been applied to coverage optimization problems, including Particle Swarm Optimization (PSO) [41], Simulated Annealing [42], Genetic Algorithms (GAs) [43], and Gray Wolf Optimizer (GWO) [44]. Recently, the Subtraction-Average-Based Optimizer (SABO), proposed by Trojovsky et al. [45], has emerged as a promising approach. The SABO utilizes a specialized arithmetic subtraction operator "$-_v$" to guide search agents, thereby mitigating dependency on specific population structures and preventing premature convergence. Since the SABO has demonstrated superior performance over traditional algorithms (e.g., PSO, GA, GWO) across multiple benchmark functions, it is selected as the baseline optimizer for this study.

The subtraction operation "$-_v$" between search agent A and search agent B is defined as follows:

$$A -_v B = sign(F(A) - F(B))(A - \vec{v} * B) \tag{14}$$

where A and B are $N \times m$ matrices, N represents the population size and m denotes the number of decision variables. $F(A)$ and $F(B)$ are the values of the fitness function of the agent A and B using Equation (8). The vector $\vec{v}$, which is used in the subtraction operation, has a dimension of m, with each component I being a random number within the range [1, 2]. The symbol "$*$" denotes the Hadamard product of two vectors.

The SABO algorithm employs the uniquely designed subtraction operator "$-_v$" to update the position of each agent in the population; thus the new position for each search agent is calculated as follows:

$$X_i^{new} = X_i + \vec{r}_i * \frac{1}{N} \sum_{j=1}^{N} (X_i -_v X_j), i = 1, 2, \ldots, N \tag{15}$$

where X_i^{new} is the new position for the search agent X_i, and $\vec{r}_i$ is a vector of the dimension m, in which components have a normal distribution with the values from the interval [0, 1].

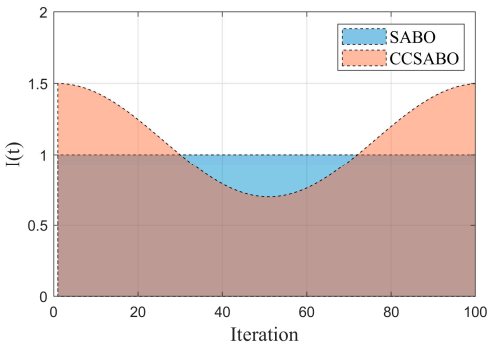
To determine whether to update the agent's position, a greedy selection mechanism is applied. If the new position results in a lower fitness value (indicating improvement), it is accepted; otherwise, the previous position is retained, as described in Equation (16):

$$X_i = \begin{cases} X_i^{new}, & F(X_i^{new}) < F(X_i) \\ X_i, & \text{else} \end{cases} \tag{16}$$

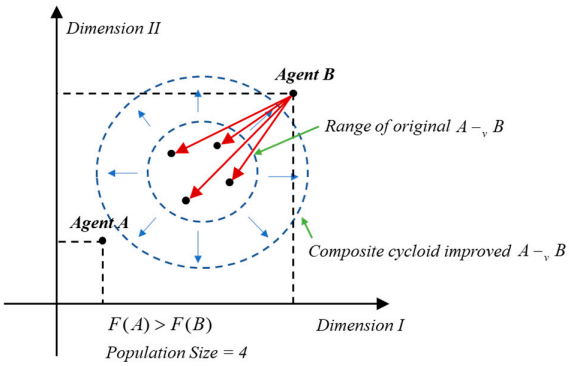
The vector $\vec{v}$ plays a crucial role in determining the step length that guides a search agent toward better-performing peers. In this study, we integrate a composite cycloid optimization [46] approach to refine the generation of $\vec{v}$. As shown in Figure 13, the comparison of the $\vec{v}$ values and $A -_v B$ values before and after the improvement is presented. It can be observed that the standard SABO utilizes a fixed $\vec{v}$, resulting in a fixed movement range for each iteration. In contrast, the $\vec{v}$ value improved by the composite cycloid strategy is able to change dynamically during the optimization process. This dynamic adjustment increases the $\vec{v}$ value while simultaneously expanding the range of the $A -_v B$ value, thereby enhancing the algorithm's exploration capability. This appropriately expands the search space during both the initial exploration and final exploitation stages to enhance global search capabilities. The improved parameter $\vec{v}'$, derived via the composite cycloid method, is formulated as:

$$I(t) = \text{rand}[1,2] + 0.5 - 0.8 \cdot \left(\frac{1}{2} - \frac{1}{2}\cos\left(\frac{2\pi t}{T_{Iter}}\right)\right) \quad t \in [1, T_{Iter}] \tag{17}$$

where t is the current iteration count, T_{Iter} is the maximum number of iterations, and rand[1,2] denotes the random number in the range of [1,2].



(**a**)



(**b**)

Figure 13. Comparison of SABO and CCSABO. (**a**) Comparison of the range of standard $\vec{v}$ and the improved $\vec{v}'$. (**b**) Comparison of the range of standard $A -_v B$ and the improved $A -_v B$. Red arrows indicate new population migration directions, while blue arrows represent expanded population distribution ranges.

The optimal control strategy is calculated based on the composite cycloid SABO (CCASBO), with the implementation steps shown as a pseudocode in Algorithm 1.

Algorithm 1. Pseudocode of the CCSABO

Start CCSABO
1. Input the information: variables, objective function, and constraints.
2. Initialize the population size (N_{Popu}), the number of iterations (T_{Iter}).
3. Generate the initial search agents′ matrix (x_i) at random.
$x_i = [u_i, v_i],\ u_i \in [u_{\min}, u_{\max}],\ v_i \in [v_{\min}, v_{\max}]$
4. Evaluate the objective function $f(x)$.
5. **For** $t = 1$ to T
6. **For** $i = 1$ to N
7. Calculate the parameter optimized by composite cycloid through Equation (17).
8. Calculate the new proposed position for search agent through Equation (15).
9. Update the best position and best fitness through Equation (16).
10. **end for**
11. Save the best candidate solution so far.
12. **end for**
13. Output optimal solution obtained with the CCSABO.
End CCSABO

5. Verification and Discussion

To verify the feasibility and superiority of the optimization framework proposed, two simulation tests were conducted comparing six different approaches: the Line Sweep strategy (LS), the Reciprocating Sweep strategy (RS), and the Reciprocating Sweep strategy optimized by SABO, CCSABO, GWO, and PSO. By minimizing the fitness function in Equation (8), the optimal forward velocity u and sweep velocity v were obtained, enabling the robot to perform uniform and efficient cleaning. The simulations were executed on a Windows 10 operating system powered by an Intel® Core™ i5-9300H processor.

5.1. Analysis of Simulation Parameters

The two simulation tests shared identical coverage area dimensions and optimization parameters, as detailed in Table 4. The velocity constraints for u and v were set based on the operational limits of the robot's cylinder and motor, respectively. To assess robustness, two different nozzle configurations were employed: Test 1 utilized parameters derived from the cavitation jet coverage model in Section 3.1, while Test 2 used adjusted parameters to evaluate the impact of nozzle variations on optimization performance. Detailed nozzle parameters are provided in Table 5.

Table 4. Parameter settings for cleaning simulation and optimization algorithms.

Parameter	Symbol	Parameters
Area size	$L \times W$	500 mm × 600 mm
Length of the spray gun	l_1	400 mm
Cylinder stroke	l_2	200 mm
Number of sampling points	N_p	200
Fitness function coefficients	k_{f1}, k_{f2}, k_{f3}	1.2, 1.5, 1
Forward velocity range	$u_{\min}, u_{\max}$	20 mm/s, 200 mm/s
Lateral velocity range	$v_{\min}, v_{\max}$	0 mm/s, 3000 mm/s
maximum number of iterations	T_{Iter}	100
Population size	N_{Popu}	10
Desired cleaning depth	$d_{desired}$	6 mm/4 mm

Table 5. Nozzle parameters for the two simulation experiments.

Parameters	Symbol	Test 1 Parameters	Test 2 Parameters
Standoff distance	d_1	90 mm	45 mm
Jet coverage radius	R	40 mm	26 mm
Standard deviation Gaussian function	s	9.5	5
Jet spread angle	α	25°	30°
Maximum cleaning efficiency	μ_m	0.17	0.2
Relation coefficient	τ	10 mm	15 mm

To determine the normalization constants $f_i(x)_{\min}$ and $f_i(x)_{\max}$ in Equation (9), computations were performed using parameter sets from both Test 1 and Test 2 across a range of uniformly selected lateral and forward velocities. The resulting fitness value surfaces are illustrated in Figure 14.

As shown in Figure 14a,b, the lateral velocity has a negligible effect on the cleaning depth fitness f_1. This is because lateral velocity does not influence the coverage time per unit area and, consequently, does not significantly alter the total accumulated cleaning depth. In contrast, as forward velocity increases, f_1 initially decreases and then increases. This behavior occurs because higher forward velocity reduces the dwell time; f_1 reaches its minimum when the forward velocity is optimized such that the actual cleaning depth precisely matches the desired target.

Figure 14c,d indicate that both lateral and forward velocities significantly influence the uniformity fitness f_2. It has been demonstrated that as the lateral velocity increases, the fitness value decreases, indicating an improvement in uniformity. Conversely, a higher forward velocity results in a higher fitness value, corresponding to poorer uniformity. This trend is particularly pronounced when the lateral velocity is low.

Figure 14e,f reveal that lateral velocity has no impact on the time fitness f_3, whereas a higher forward velocity directly leads to a smaller f_3, reflecting improved cleaning efficiency. This observation aligns with intuitive expectations, implying that the velocity of the lateral mechanism does not affect the total cleaning duration. Instead, cleaning efficiency is solely determined by the robot's forward velocity, where higher velocity yield greater efficiency.

This analysis demonstrates the rationality of the fitness function design. Based on these calculations, the boundary values for normalization were determined and are listed in Table 6. Notably, to mitigate the influence of outliers and enhance convergence stability, the determination of $f_1(x)_{\min/\max}$ involved trimming the top and bottom 10% of extreme values, whereas the bounds for $f_2(x)_{\min/\max}$ and $f_3(x)_{\min/\max}$ were adopted directly.

Table 6. Parameter values used for normalization.

Symbol	Test 1 Parameters	Test 2 Parameters
$f_1(x)_{\min}$	50	50
$f_1(x)_{\max}$	600	1000
$f_2(x)_{\min}$	0	0
$f_2(x)_{\max}$	1	1
$f_3(x)_{\min}$	25	25
$f_3(x)_{\max}$	250	250

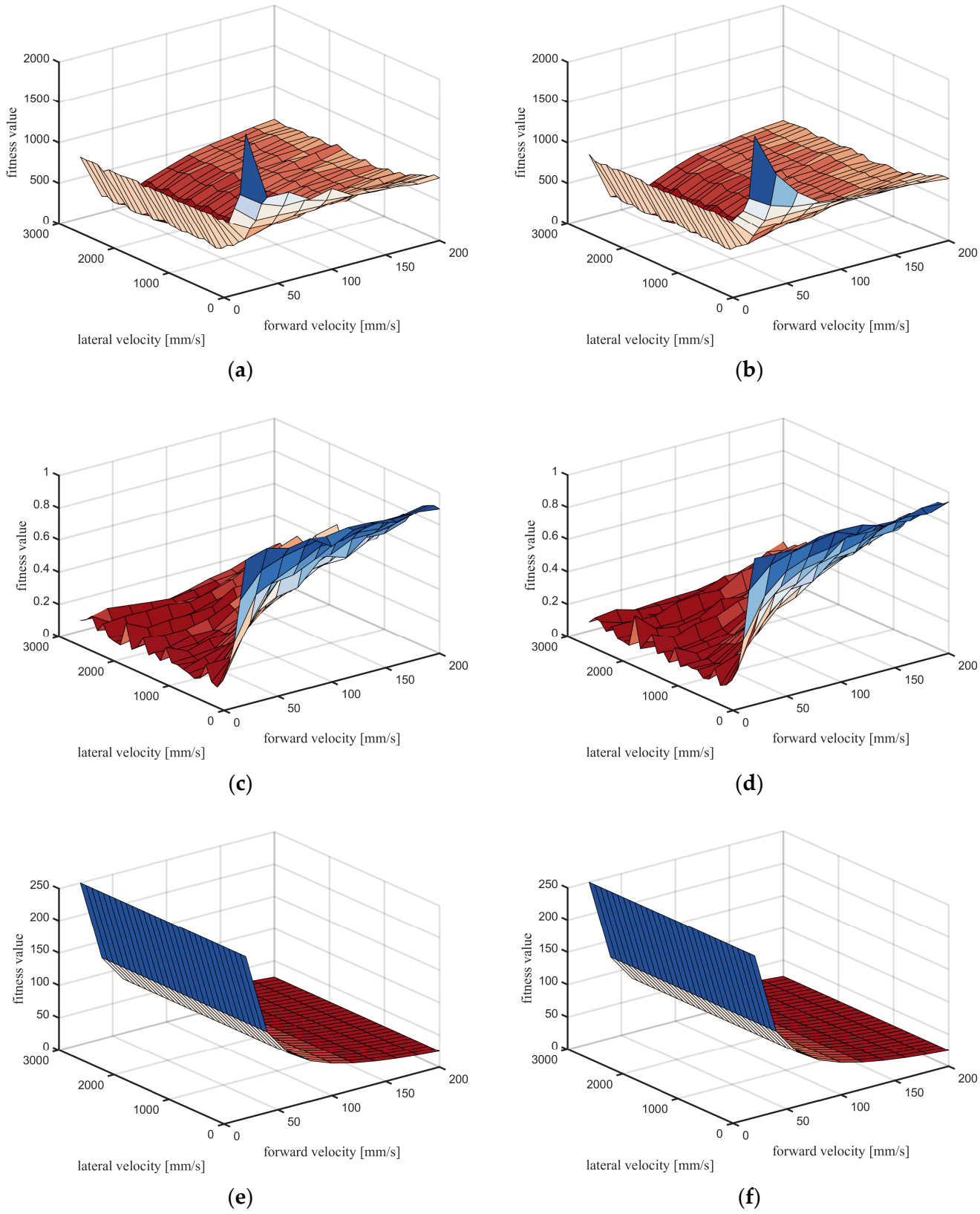


Figure 14. Distribution of fitness function values relative to forward and lateral velocities. (**a**) f_1 in test 1; (**b**) f_1 in test 2; (**c**) f_2 in test 1; (**d**) f_2 in test 2; (**e**) f_3 in test 1; (**f**) f_3 in test 2.

5.2. Simulation Results

The convergence curves for Test 1 and Test 2 are depicted in Figures 15a and 15b, respectively. These curves illustrate the iterative performance of SABO, CCSABO, GWO,

and PSO over 100 iterations. In the later stages of the iterative process, the fitness values of SABO hardly change, while CCSABO is able to achieve further optimization by increasing the exploration range. In both test scenarios, CCSABO demonstrates superior global optimization capability, converging to a lower fitness value more rapidly than the comparative algorithms.

The cleaning coverage simulations for Test 1 are shown in Figure 16, where blue represents varying levels of cleanliness (depth) and red indicates uncleaned areas. The correlation between color and cleaning depth is provided in Figure 16g, with black lines tracing the nozzle's sweep path. Figure 16a shows that the unoptimized LS method results in a poor coverage rate. Figure 16b indicates that while the unoptimized RS method significantly improves coverage, distinct triangular uncleaned regions remain. Figure 16c–f demonstrate that optimizing the RS parameters using different algorithms substantially enhances uniformity. Specifically, Figure 16d reveals that CCSABO achieves the most effective coverage with the highest uniformity.

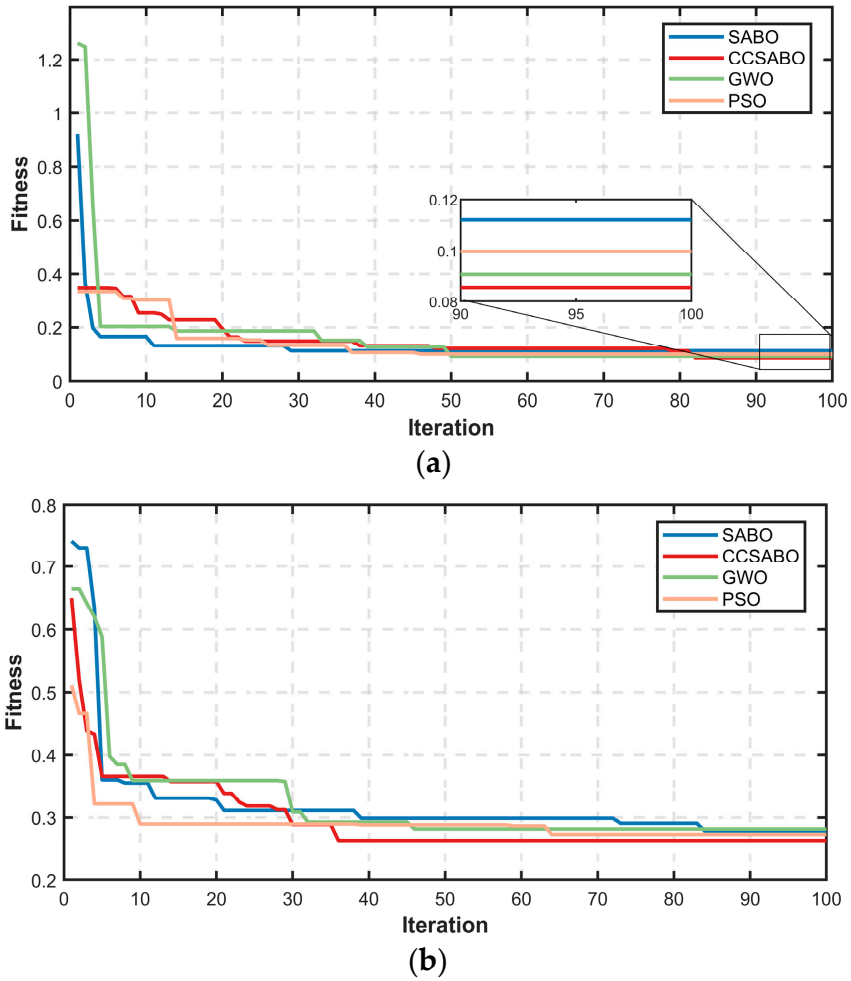


Figure 15. Fitness value convergence curves for the four optimization algorithms. (**a**) Test 1; (**b**) Test 2.

The results for Test 2, presented in Figure 17, mirror those of Test 1, confirming CCSABO's superior performance. A key difference in Test 2 is the smaller jet coverage radius, which necessitates a higher lateral velocity to ensure uniform coverage. It is also noteworthy that the optimization results tend to favor increased forward velocity to maximize efficiency (f_3), provided it is coordinated with the lateral velocity to maintain uniformity (f_2) and meet the desired cleaning depth (f_1).

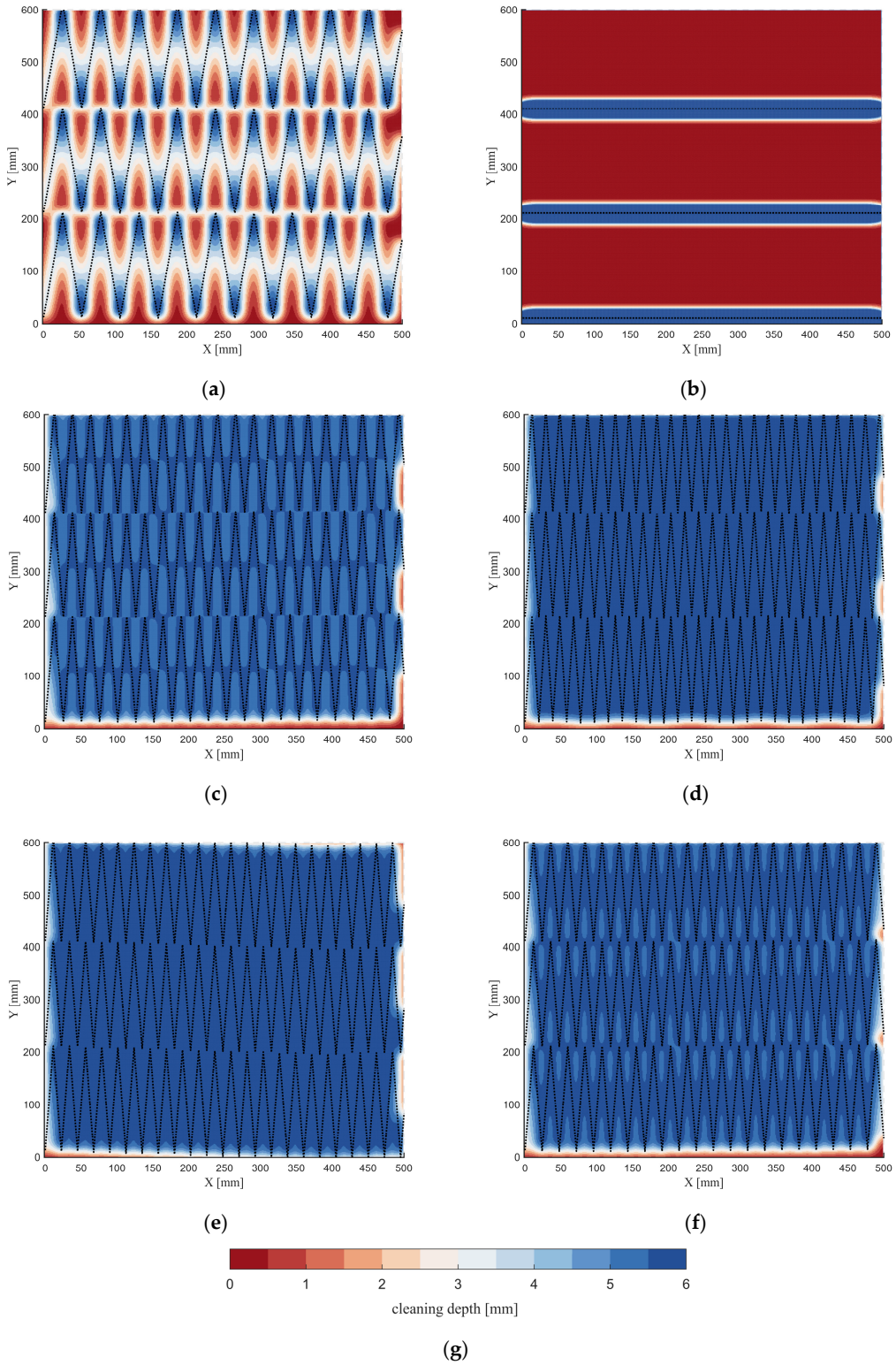


Figure 16. Comparison of cleaning effectiveness using different strategies in Test 1. (**a**) LS without optimized; (**b**) RS without optimized; (**c**) RS optimized by SABO; (**d**) RS optimized by CCSABO; (**e**) RS optimized by GWO; (**f**) RS optimized by PSO; (**g**) The correspondence between cleaning depth and color. ((**a**): u = 0 mm/s, v = 200 mm/s, (**b**): u = 200 mm/s, v = 1500 mm/s, (**c**): u = 113 mm/s, v = 1800 mm/s, (**d**): u = 105 mm/s, v = 2118 mm/s, (**e**): u = 1839 mm/s, v = 103 mm/s, (**f**): u = 1820 mm/s, v = 109 mm/s, desired depth = 6 mm).

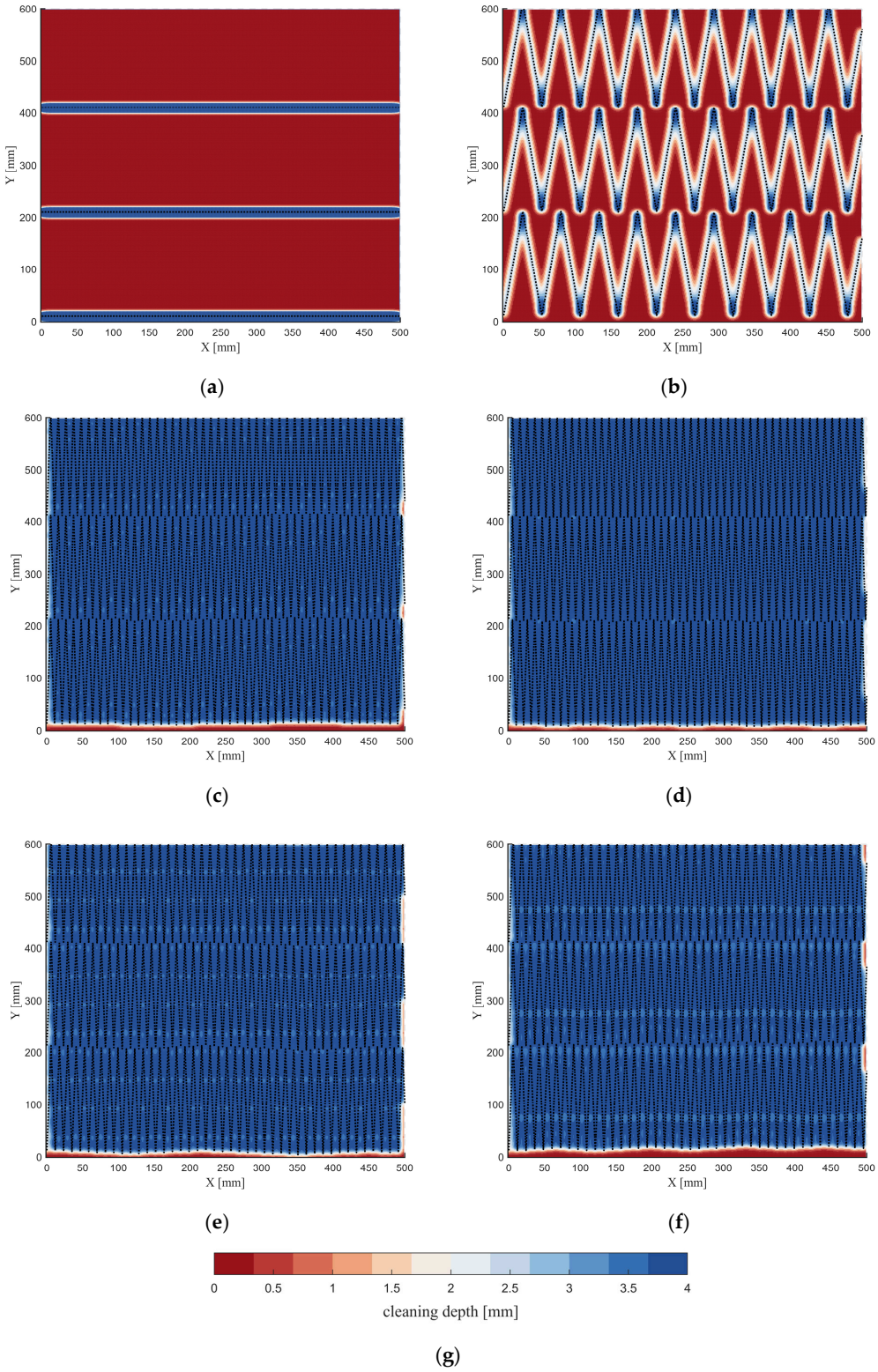


Figure 17. Comparison of cleaning effectiveness using different strategies in Test 2. (**a**) LS without optimized; (**b**) RS without optimized; (**c**) RS optimized by SABO; (**d**) RS optimized by CCSABO; (**e**) RS optimized by GWO; (**f**) RS optimized by PSO; (**g**) The correspondence between cleaning depth and color. ((**a**): u = 0 mm/s, v = 200 mm/s, (**b**): u = 200 mm/s, v = 1500 mm/s, (**c**): u = 61 mm/s, v = 2297 mm/s, (**d**): u = 60 mm/s, v = 2302 mm/s, (**e**): u = 58 mm/s, v = 2037 mm/s, (**f**): u = 61 mm/s, v = 2015 mm/s, desired depth = 4 mm).

To statistically analyze cleaning performance, 200 points were randomly sampled within the coverage area. Figure 18 presents the boxplots of their cleaning depths, where

red lines represent the median and gray lines indicate the desired target depth. The cleaning depths for the unoptimized LS and RS strategies are significantly lower than the target. In contrast, the optimized strategies show marked improvement. CCSABO stands out with the tightest distribution of cleaning depths around the desired value, evidencing superior uniformity.

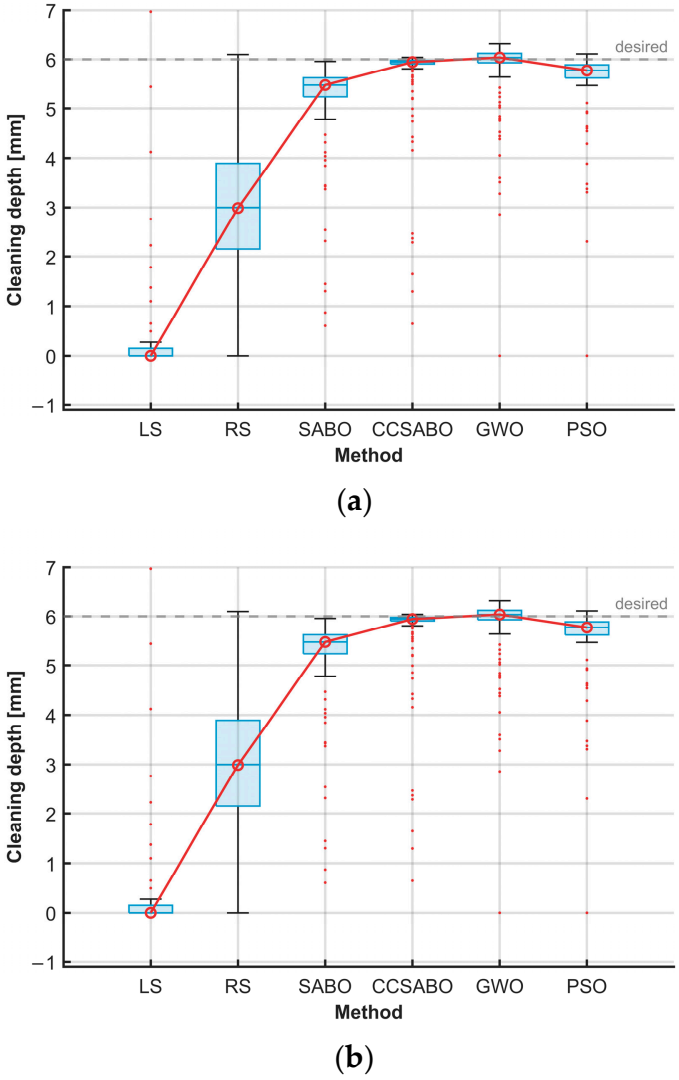


Figure 18. Boxplot distribution of cleaning depths for different strategies. (**a**) Test 1; (**b**) Test 2.

The results for the coverage rate, uniformity, median, and time consumption are presented in Tables 7 and 8, with the best results highlighted in gray. In this study, effective cleaning coverage is defined as achieving a cleaning depth within ±20% of the desired target depth. Uniformity was calculated using the formula shown in (11). The best coverage rate reached 98% and 99%, respectively, through CCSABO, and its uniformity is also the smallest, indicating that it performs the best in terms of uniform coverage. Moreover, CCSABO's median value is close to the desired value, offering an excellent coverage effect. In conclusion, it is evident that the optimized algorithms, including GWO and PSO, result in a significantly increased coverage rate, median, and uniformity. However, the CCSABO approach provided superior performance, validating the effectiveness of the proposed discrete coverage strategy and CCSABO optimization method.

Table 7. Experimental results of four cleaning strategies in Test 1. The best results are highlighted with a gray background.

Algorithm	Coverage	Median	Uniformity	Time Spent
LS	17%	0.00 mm	0.844	25.0 s
RS	56%	3.21 mm	0.155	25.0 s
SABO	96%	5.51 mm	0.026	43.9 s
CCSABO	98%	5.96 mm	0.015	47.3 s
GWO	98%	6.05 mm	0.017	48.3 s
PSO	98%	5.74 mm	0.020	46.1 s

Table 8. Experimental results of four cleaning strategies in Test 2. The best results are highlighted with a gray background.

Algorithm	Coverage Rate	Median Depth	Uniformity	Time Spent
LS	12%	0.16 mm	0.899	25.0 s
RS	25%	1.37 mm	0.473	25.0 s
SABO	98%	3.83 mm	0.017	81.7 s
CCSABO	99%	3.94 mm	0.011	83.6 s
GWO	98%	3.95 mm	0.013	83.9 s
PSO	96%	3.86 mm	0.032	82.1 s

Although the CCSABO algorithm requires slightly longer processing time, the primary objective within the optimization framework proposed is to minimize damage to the expensive anti-fouling coating (uniformity). Therefore, the slight increase in processing time is acceptable given the significant improvements in safety and quality.

In conclusion, while all optimized algorithms (including GWO and PSO) significantly improved coverage, median depth, and uniformity compared to baseline strategies, CCSABO consistently provided the superior performance. This validates the effectiveness of the proposed optimization framework in non-uniform cavitation erosion characteristics for hull cleaning applications.

6. Conclusions

This paper presents a comprehensive coverage optimization framework for underwater ship hull cleaning robots, explicitly addressing the challenges posed by the inherent non-uniform cavitation erosion characteristics of cleaning jets. By integrating hydrodynamic analysis with kinematic optimization, the proposed framework achieves efficient, uniform, and damage-free cleaning. The key contributions and findings are summarized as follows:

(1) Characterization of Non-Uniform Erosion: The complex flow field dynamics of the cavitation nozzle were elucidated using the Stress-Blended Eddy Simulation (SBES) turbulence model. The simulation results effectively quantified the non-uniform energy distribution within the jet, identifying the optimal standoff distance as approximately 90 mm, with a jet spread angle of 25° and a coverage radius of 40 mm. These parameters provide the hydrodynamic baseline for precision cleaning.

(2) Establishment of Erosion-Motion Mapping Model: To bridge the gap between jet hydrodynamics and robotic kinematics, a Gaussian mapping model was constructed. This model accurately characterizes the cleaning efficiency distribution (with $R^2 > 0.98$ and $RMSE < 0.06$), allowing for the precise correlation of the robot's lateral velocity v and forward velocity u with the erosion depth. This step effectively resolves the difficulty of predicting removal depth caused by irregular jet energy.

(3) Optimization via CCSABO: To address the multi-objective optimization problem of maximizing coverage while minimizing hull damage, the Composite Cycloid Subtraction-Average-Based Optimizer (CCSABO) was introduced. Numerical simulations demonstrate that CCSABO significantly outperforms traditional algorithms (PSO and GWO). It successfully synchronizes the robot's motion parameters, achieving a coverage rate of 99% and an improved uniformity index of 0.011. This performance ensures that the cleaning process effectively removes fouling without causing substrate damage due to local over-cleaning.

It should be noted that CCSABO achieves superior cleaning uniformity, which is a key factor in preventing damage. This process takes a little more time than traditional methods, such as GWO. This trade-off is reasonable given the high value of hull assets; however, future work will aim to further optimize the time consumption of the algorithm to improve its efficiency. We will also focus on prototype testing to validate the practicality of this strategy in real-world marine environments and further optimizing the nozzle incidence angle to enhance cleaning adaptability on complex curved surfaces.

Author Contributions: Conceptualization, Z.L. and Y.W.; methodology, Z.L.; software, Y.W.; investigation, Y.W.; writing—original draft preparation, Z.L.; writing—review and editing, C.J.; visualization, Z.Y.; supervision, Z.Y.; project administration, C.J. All authors have read and agreed to the published version of the manuscript.

Funding: This research received no external funding.

Data Availability Statement: The data presented in this study are available on request from the corresponding author due to privacy.

Conflicts of Interest: The authors declare no conflicts of interest.

References

1. Davidson, I.; Scianni, C.; Hewitt, C.; Everett, R.; Holm, E.; Tamburri, M.; Ruiz, G. Mini-Review: Assessing the Drivers of Ship Biofouling Management—Aligning Industry and Biosecurity Goals. *Biofouling* **2016**, *32*, 411–428. [CrossRef]
2. Adland, R.; Cariou, P.; Jia, H.; Wolff, F.-C. The Energy Efficiency Effects of Periodic Ship Hull Cleaning. *J. Clean. Prod.* **2018**, *178*, 1–13. [CrossRef]
3. Nassiraei, A.A.F.; Sonoda, T.; Ishii, K. Development of Ship Hull Cleaning Underwater Robot. In Proceedings of the 2012 Fifth International Conference on Emerging Trends in Engineering and Technology (ICETET 2012), Himeji, Japan, 5–7 November 2012; pp. 157–162.
4. Iborra, A.; Pastor, J.A.; Alonso, D.; Alvarez, B.; Ortiz, F.J.; Navarro, P.J.; Fernández, C.; Suardiaz, J. A Cost-Effective Robotic Solution for the Cleaning of Ships' Hulls. *Robotica* **2010**, *28*, 453–464. [CrossRef]
5. Lee, M.H.; Park, Y.D.; Park, H.G.; Park, W.C.; Hong, S.; Lee, K.S.; Chun, H.H. Hydrodynamic Design of an Underwater Hull Cleaning Robot and Its Evaluation. *Int. J. Nav. Archit. Ocean Eng.* **2012**, *4*, 335–352. [CrossRef]
6. Wang, B.; Ni, Z.; Shen, Y.; Zhang, S.; Shen, Q.; Niu, X.W. Design and Analysis of a Wheel-Leg Compound Variable Curvature Ship Hull Cleaning Robot. *Ocean Eng.* **2022**, *266*, 112755. [CrossRef]
7. Chen, L.; Cui, R.; Yan, W.; Xu, H.; Zhao, H.; Li, H. Design and Climbing Control of an Underwater Robot for Ship Hull Cleaning. *Ocean Eng.* **2023**, *274*, 114024. [CrossRef]
8. Wei, K.; Zhang, Z.; Zhou, Z. Design of a New Composite Underwater Hull Cleaning Robot. *J. Sea Res.* **2024**, *198*, 102488. [CrossRef]
9. Albitar, H.; Dandan, K.; Ananiev, A.; Kalaykov, I. Underwater Robotics: Surface Cleaning Technics, Adhesion and Locomotion Systems. *Int. J. Adv. Robot. Syst.* **2016**, *13*, 7. [CrossRef]
10. Davidson, I.C.; McCann, L.D.; Sytsma, M.D.; Ruiz, G.M. Interrupting a Multi-Species Bioinvasion Vector: The Efficacy of in-Water Cleaning for Removing Biofouling on Obsolete Vessels. *Mar. Pollut. Bull.* **2008**, *56*, 1538–1544. [CrossRef]
11. Cheng, H.; Long, X.; Ji, B.; Peng, X.; Farhat, M. A New Euler-Lagrangian Cavitation Model for Tip-Vortex Cavitation with the Effect of Non-Condensable Gas. *Int. J. Multiph. Flow* **2021**, *134*, 103441. [CrossRef]
12. Long, X.; Cheng, H.; Ji, B.; Arndt, R.E.A.; Peng, X. Large Eddy Simulation and Euler-Lagrangian Coupling Investigation of the Transient Cavitating Turbulent Flow around a Twisted Hydrofoil. *Int. J. Multiph. Flow* **2018**, *100*, 41–56. [CrossRef]

13. Zhu, R.; Zhu, H.; Zhang, X. Numerical Investigation about the Unsteady Behavior of a Free Submerged Cavitation Jet Using the SBES Approach. *Ocean Eng.* **2023**, *281*, 115010. [CrossRef]
14. Muthugala, M.A.V.J.; Samarakoon, S.M.B.P.; Elara, M.R. Toward Energy-Efficient Online Complete Coverage Path Planning of a Ship Hull Maintenance Robot Based on Glasius Bio-Inspired Neural Network. *Expert Syst. Appl.* **2022**, *187*, 115940. [CrossRef]
15. Armagan, M. Cutting of St37 Steel Plates in Stacked Form with Abrasive Water Jet. *Mater. Manuf. Process.* **2021**, *36*, 1305–1313. [CrossRef]
16. Mahmud, M.S.A.; Abidin, M.S.Z.; Buyamin, S.; Emmanuel, A.A.; Hasan, H.S. Multi-Objective Route Planning for Underwater Cleaning Robot in Water Reservoir Tank. *J. Intell. Robot. Syst.* **2021**, *101*, 9. [CrossRef]
17. Anh, V.L.; Veerajagadheswar, P.; Kyaw, P.T.; Muthugala, M.A.V.J.; Elara, M.R.; Kuma, M.; Nguyen, H.K.N. Towards Optimal Hydro-Blasting in Reconfigurable Climbing System for Corroded Ship Hull Cleaning and Maintenance. *Expert Syst. Appl.* **2021**, *170*, 114519. [CrossRef]
18. Ghanta, S.; Rayguru, M.M.; Pathmakumar, T.; Kalimuthu, M.; Elara, M.R.; Sheu, B.J. Uniform Hydro Blasting for Ship Hull Maintenance: A Multi-Objective Optimization Framework. *Ocean Eng.* **2021**, *242*, 109977. [CrossRef]
19. Liu, B.; Pan, Y.; Ma, F. Pulse Pressure Loading and Erosion Pattern of Cavitating Jet. *Eng. Appl. Comp. Fluid Mech.* **2020**, *14*, 136–150. [CrossRef]
20. Madanipour, V.; Najafi, F. Modal Analysis of Underwater Hull Cleaning Robot Considering Environmental Interaction. *Ocean Eng.* **2023**, *273*, 113821. [CrossRef]
21. Fang, Z.; Ji, Z.; Kang, D.; Chen, Y.; Zhang, X.; Wang, S.; Xiong, T. Cavitation Damage Characteristics Following Marine Fouling Cleaning by a Self-Excited Oscillation Cavitation Waterjet. *Appl. Ocean Res.* **2023**, *139*, 103692. [CrossRef]
22. Zhang, Y.; He, C.; Sun, L. Optimization of an Ejector to Mitigate Cavitation Phenomena with Coupled CFD/BP Neural Network and Particle Swarm Optimization Algorithm. *Prog. Nucl. Energy* **2022**, *153*, 104412. [CrossRef]
23. Apte, D.; Razaaly, N.; Fang, Y.; Ge, M.; Sandberg, R.; Coutier-Delgosha, O. A Novel Data-Driven Method for Augmenting Turbulence Modeling for Unsteady Cavitating Flows. *Int. J. Heat Fluid Flow* **2025**, *115*, 109847. [CrossRef]
24. Chen, Y.; Hu, Y.; Zhang, S. Structure Optimization of Submerged Water Jet Cavitating Nozzle with a Hybrid Algorithm. *Eng. Appl. Comput. Fluid Mech.* **2019**, *13*, 591–608. [CrossRef]
25. Wu, X.-Y.; Zhang, Y.-Q.; Tan, Y.-W.; Li, G.-S.; Peng, K.-W.; Zhang, B. Flow-Visualization and Numerical Investigation on the Optimum Design of Cavitating Jet Nozzle. *Pet. Sci.* **2022**, *19*, 2284–2296. [CrossRef]
26. Hong, F.; Yuan, J.; Zhou, B.; Li, Z. Modeling of Unsteady Structure of Sheet/Cloud Cavitation around a Two-Dimensional Stationary Hydrofoil. *Proc. Inst. Mech. Eng. Part E J. Process Mech. Eng.* **2017**, *231*, 455–469. [CrossRef]
27. Long, X.; Cheng, H.; Ji, B.; Arndt, R.E.A. Numerical Investigation of Attached Cavitation Shedding Dynamics around the Clark-Y Hydrofoil with the FBDCM and an Integral Method. *Ocean Eng.* **2017**, *137*, 247–261. [CrossRef]
28. Liu, C.; Yan, Q.; Wood, H.G. Numerical Investigation of Passive Cavitation Control Using a Slot on a Three-Dimensional Hydrofoil. *Int. J. Numer. Methods Heat Fluid Flow* **2019**, *30*, 3585–3605. [CrossRef]
29. Yang, Y.; Shi, W.; Tan, L.; Li, W.; Chen, S.; Pan, B. Numerical Research of the Submerged High-Pressure Cavitation Water Jet Based on the RANS-LES Hybrid Model. *Shock Vib.* **2021**, *2021*, 6616718. [CrossRef]
30. Liu, W.; Kang, Y.; Zhang, M.; Wang, X.; Li, D. Self-Sustained Oscillation and Cavitation Characteristics of a Jet in a Helmholtz Resonator. *Int. J. Heat Fluid Flow* **2017**, *68*, 158–172. [CrossRef]
31. Liu, W.; Kang, Y.; Wang, X.; Liu, Q.; Fang, Z. Integrated CFD-Aided Theoretical Demonstration of Cavitation Modulation in Self-Sustained Oscillating Jets. *Appl. Math. Model.* **2020**, *79*, 521–543. [CrossRef]
32. Fang, Z.; Zeng, F.; Xiong, T.; Wei, W.; Jiang, P.; Wu, Q.; Wang, Y.; Fei, Y. Large Eddy Simulation of Self-Excited Oscillation inside Helmholtz Oscillator. *Int. J. Multiph. Flow* **2020**, *126*, 103253. [CrossRef]
33. Choi, J.-K.; Jayaprakash, A.; Chahine, G.L. Scaling of Cavitation Erosion Progression with Cavitation Intensity and Cavitation Source. *Wear* **2012**, *278*, 53–61. [CrossRef]
34. Zhong, X.; Dong, J.; Liu, M.; Meng, R.; Li, S.; Pan, X. Experimental Study on Ship Fouling Cleaning by Ultrasonic-Enhanced Submerged Cavitation Jet: A Preliminary Study. *Ocean Eng.* **2022**, *258*, 111844. [CrossRef]
35. Liu, B.; Ma, F. Erosion Behavior of Aluminum by an Inclined Cavitating Jet. *Wear* **2021**, *474*, 203751. [CrossRef]
36. Liu, H.; Cao, Z.; Xie, C.; Chen, G.; Li, D.; Wang, J. Research on Erosion Characteristics of a Novel Cavitation Nozzle under Nonsubmerged Condition. *Proc. Inst. Mech. Eng. Part C-J. Eng. Mech. Eng. Sci.* **2021**, *235*, 988–998. [CrossRef]
37. Chen, W.; Yang, P.; Zhao, W.; Wei, L. Improved Ant Lion Optimizer for Coverage Optimization in Wireless Sensor Networks. *Wirel. Commun. Mob. Comput.* **2022**, *2022*, 8808575. [CrossRef]
38. Yakoubi, M.A.; Laskri, M.T. The Path Planning of Cleaner Robot for Coverage Region Using Genetic Algorithms. *J. Innov. Digit. Ecosyst.* **2016**, *3*, 37–43. [CrossRef]
39. Zeng, C.; Qin, T.; Tan, W.; Lin, C.; Zhu, Z.; Yang, J.; Yuan, S. Coverage Optimization of Heterogeneous Wireless Sensor Network Based on Improved Wild Horse Optimizer. *Biomimetics* **2023**, *8*, 70. [CrossRef] [PubMed]

40. Jain, R.; Chiu, D.; Hawe, W. *A Quantitative Measure of Fairness and Discrimination for Resource Allocation in Shared Computer Systems*; Research Report DEC-TR-301; Digital Equipment Corporation: Hudson, MA, USA, 1984; Available online: http://www.cs.wustl.edu/ jain/papers/ftp/fairness.pdf (accessed on 21 January 2026).
41. Liu, A.; Yuan, Y.; Yin, H.; Zhao, H.; Fu, X. Optimization of LED Array Spatial Coverage Characteristics in Underwater Wireless Optical Communication. *J. Mar. Sci. Eng.* **2023**, *11*, 253. [CrossRef]
42. Liu, H.; Lin, Z.; Xu, Y.; Chen, Y.; Pu, X. Coverage Uniformity with Improved Genetic Simulated Annealing Algorithm for Indoor Visible Light Communications. *Opt. Commun.* **2019**, *439*, 156–163. [CrossRef]
43. Pathmakumar, T.; Rayguru, M.M.; Ghanta, S.; Kalimuthu, M.; Elara, M.R. An Optimal Footprint Based Coverage Planning for Hydro Blasting Robots. *Sensors* **2021**, *21*, 1194. [CrossRef]
44. Wang, S.; Yang, X.; Wang, X.; Qian, Z. A Virtual Force Algorithm-Levy-Embedded Grey Wolf Optimization Algorithm for Wireless Sensor Network Coverage Optimization. *Sensors* **2019**, *19*, 2735. [CrossRef]
45. Trojovsky, P.; Dehghani, M. Subtraction-Average-Based Optimizer: A New Swarm-Inspired Metaheuristic Algorithm for Solving Optimization Problems. *Biomimetics* **2023**, *8*, 149. [CrossRef]
46. Dosa, G.; Newman, N.; Tuza, Z.; Voloshin, V. Coloring Properties of Mixed Cycloids. *Symmetry* **2021**, *13*, 1539. [CrossRef]

Disclaimer/Publisher's Note: The statements, opinions and data contained in all publications are solely those of the individual author(s) and contributor(s) and not of MDPI and/or the editor(s). MDPI and/or the editor(s) disclaim responsibility for any injury to people or property resulting from any ideas, methods, instructions or products referred to in the content.